Electromagnetics and Antenna Technology, Ch. 9

Alan J. Fenn

Senior Staff Member
Lincoln Laboratory
Massachusetts Institute of Technology
244 Wood Street
Lexington, MA 02420

June 3, 2017

Published document will have the following statement:

9

3D-Printed Non-Planar Circular Patch Array Antenna

9.1 Introduction

Patch antennas, or microstrip antennas, have been explored extensively for a large variety of antenna designs for single elements and in phased arrays [1]. These antennas are particularly useful in applications requiring a thin profile or antennas that must conform to the surface of a curved structure. Common patch antenna shapes are rectangular, square, and circular [1-7]. Patch antennas are used for linear, dual linear or circular polarization applications. Patch antennas can be fed with an electrically conducting pin or a microstrip line directly connected to the patch or proximity coupled to the patch. In this chapter, the focus is on the design, analysis, and measurements of a conformal array of circular patch antennas. A non-planar, conformal array antenna is described that uses a combination of 3D printer and copper plating techniques, referred to as an additive manufacturing process. Circular patch antenna elements are copper plated onto a 3D printed dielectric substrate made of ABS-M30 material. Measured and simulated element reflection coefficient, element gain patterns, and array scanned beam radiation patterns at L band are shown.

Nonplanar phased arrays are of interest for applications requiring antennas that are conformal to the skin surface of a structure. Using 3D printing techniques [8-20], also referred to as additive manufacturing, structures that can be considered can have an arbitrary shape such as a cylinder, cone, sphere, or other more general irregular shapes. 3D printer technology for fabrication of electronic circuitry and antennas is a subject of great interest for rapid prototyping and has been explored by a number of researchers in the last few years. A conformal array can offer 1) lower aerodynamic drag, 2) reduced radar cross section (RCS), 3) enhanced angular coverage, and 4) potentially lower fabrication and installation costs. Low-profile microstrip patch array antenna elements on a dielectric substrate are a candidate for these applications [21].

Nonplanar microstrip patch antenna arrays using 3D printer and copper plating techniques have recently been explored [19]. Element reflection coefficient, element gain and phase patterns have been measured and simulated, and array radiation patterns were generated by superposition for an example L-band array.

The chapter is organized as follows. Section 9.2 describes the theory for circular patch antennas. An example moment method simulation for a single circular patch antenna is given in Section 9.3. Section 9.4 describes the design and fabrication of a nonplanar array with a circular arc shape and describes the array simulation model. Section 9.4 compares measured and simulated results. Section 9.5 has a summary.

9.2 Circular Patch Antenna Theory

Figure 9.1 shows a diagram of a circular patch antenna over a ground plane. The circular electrically conducting patch has radius a and is located on a

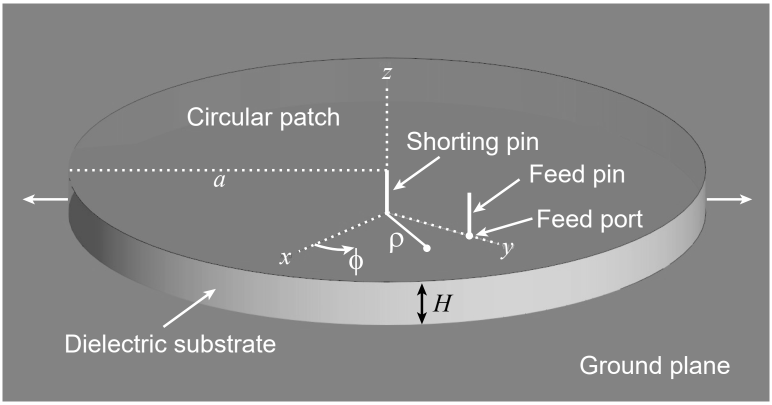

Figure 9.1 Circular patch antenna diagram.

dielectric substrate with height H and dielectric constant ϵ_r. This conducting patch geometry has been analyzed as a circular disk resonator where a number of transverse magnetic modes TM_{nmo} [$\mathrm{TM}_{\phi,\rho,z}$] can exist. An electrically conducting feed pin located at a radial distance s from the center of the patch is used to excite the patch. An optional electrically conducting shorting pin is connected between the center of the patch and the ground plane. The dominant mode, with or without the shorting pin, is the transverse magnetic TM_{110} mode that has a null at the z axis. In the literature, the TM_{110} mode is often abbreviated by dropping the third index, that is, it is written as TM_{11}

The electric and magnetic fields inside the dielectric substrate below the circular patch are given by Derneryd [6]

$$E_z(\rho, \phi) = E_o J_n(k\rho) \cos n\phi \tag{9.1}$$

$$H_\rho(\rho, \phi) = -\frac{j\omega\epsilon n}{k^2\rho} E_o J_n(k\rho) \sin n\phi \tag{9.2}$$

$$H_\phi(\rho, \phi) = -\frac{j\omega\epsilon}{k} E_o J'_n(k\rho) \cos n\phi \tag{9.3}$$

where $J_n(X)$ is the nth order Bessel function and $J'_n(X)$ is the derivative of the nth order Bessel function. The Bessel function and its derivative are given by the following recurrence equations [22]

$$J_n(X) = \frac{X}{2n}\left(J_{n-1}(X) + J_{n+1}(X)\right) \tag{9.4}$$

$$J'_n(X) = \frac{1}{2}\left(J_{n-1}(X) - J_{n+1}(X)\right) \tag{9.5}$$

It is noted that $J_1(\rho = 0) = 0$ confirming that the E_z component has a null when the radial distance is zero.

The far-zone electric field components are given by Derneryd [6]

$$E_\theta(\theta, \phi) = -j^n k_o \frac{e^{-jk_o r}}{r} \frac{V_o a}{2} B_M(k_o a \sin\theta) \cos n\phi \tag{9.6}$$

$$E_\phi(\theta, \phi) = j^n k_o \frac{e^{-jk_o r}}{r} \frac{V_o a}{2} B_P(k_o a \sin\theta) \cos\theta \sin n\phi \tag{9.7}$$

where

$$B_P(X) = J_{n-1}(X) + J_{n+1}(X) = \frac{2n}{X} J_n(X) \tag{9.8}$$

$$B_M(X) = J_{n-1}(X) - J_{n+1}(X) = 2J'_n(X) \tag{9.9}$$

The resonant frequencies of a circular patch antenna are computed according to a cavity model as described by Derneryd [6]

$$f_{nm} = \frac{q_{nm} c}{2\pi a_{\text{eff}} \sqrt{\epsilon_r}} \tag{9.10}$$

where c is the speed of light and a_{eff} is an effective radius of the circular patch that is larger than the actual patch radius. In Equation (9.10), the parameter

q_{nm} is the mth root, or value, of J'_n that enforces the boundary condition, that is, the zeros of the derivative of the nth order Bessel function $J_n(x)$. For the dominant TM$_{11}$ mode, $q_{11} = 1.841$. The effective radius a_{eff} takes account of the fringing fields at the edge of the patch and is given in terms of the actual patch radius a by

$$a_{\text{eff}} = a\sqrt{1 + \frac{2H}{\pi a \epsilon_r}\left(\ln\frac{\pi a}{2H} + 1.7726\right)} \tag{9.11}$$

Solving Equation (9.11) for a yields the desired value for the actual patch radius, that is,

$$a = \frac{a_{\text{eff}}}{\sqrt{1 + \frac{2H}{\pi a \epsilon_r}\left(\ln\frac{\pi a}{2H} + 1.7726\right)}} \tag{9.12}$$

Assuming the patch radius is much greater than the substrate height, that is, $a/H >> 1$, Equation (9.12) gives the actual patch radius to within an error of about 2.5 percent. The feed pin spacing from the shorting pin is typically chosen to be equal to about 33 percent of the radius of the patch. A quantitative method to determine the radial location (ρ) of the feed pin is as follows.

The circular patch antenna input impedance at resonance for the TM$_{11}$ mode (with $n = 1$) is purely real and is computed in terms of the radial position ρ and patch radius a as [6]

$$Z_{\text{in}}(\rho) = \frac{1}{G_{\text{total}}}\frac{J_1^2(k\rho)}{J_1^2(ka)} \tag{9.13}$$

where G_{total} is the total antenna conductance expressed as

$$G_{\text{total}} = G_{\text{rad}} + G_{\text{dielectric}} + G_{\text{finite conductivity}} \tag{9.14}$$

where G_{rad} is the radiation conductance given by

$$G_{\text{rad}} = \frac{(k_o a)^2}{480}\int_0^{\frac{\pi}{2}}\left[B_M^2(k_o a\sin\theta) + \cos^2\theta B_P^2(k_o a\sin\theta)\right]\sin\theta d\theta \tag{9.15}$$

$G_{\text{dielectric}}$ is the dielectric conductance given by

$$G_{\text{dielectric}} = \frac{\tan\delta}{4\mu_o H f_{11}}\left[(ka)^2 - 1\right] \tag{9.16}$$

$G_{\text{finite conductivity}}$ is the equivalent conductance due to the finite conductivity σ of the metal patch antenna given by

$$G_{\text{finite conductivity}} = \frac{\pi(\pi f_{11}\mu_o)^{-3/2}}{4H^2\sqrt{\sigma}}\left[(ka)^2 - 1\right] \tag{9.17}$$

9.3 Single Planar Patch Element Simulation Example

Referring to Figure 9.1, assume a circular patch antenna with diameter 8.46 cm ($a = 4.23$ cm) and substrate thickness $H = 0.3175$ cm with a dielectric constant $\epsilon_r = 2.56$ and loss tangent $\tan\delta = 0.008$. Based on Equation (9.11) the effective patch diameter is computed as 8.83 cm, which is about 4.4% greater than the assumed patch diameter. Then, based on Equation (9.10), the resonant frequency of the TM11 mode is computed as 1.244 GHz. Assume a copper conducting patch with electrical conductivity $\sigma = 5.9 \times 10^7$ S/m at room temperature. By setting the input impedance equal to 50 ohms (real) at resonance in Equation (9.13) and iterating, the radial distance for the feed point is computed to be approximately $\rho = 1.15$ cm.

Consider Figure 9.2 that shows a simulation model of the circular patch antenna, which was analyzed with the FEKO moment method solver [23]. In this simulation, the actual feed pin radial position was $\rho = 1.232$ cm. To characterize the dominant TM11 mode generated in the patch antenna

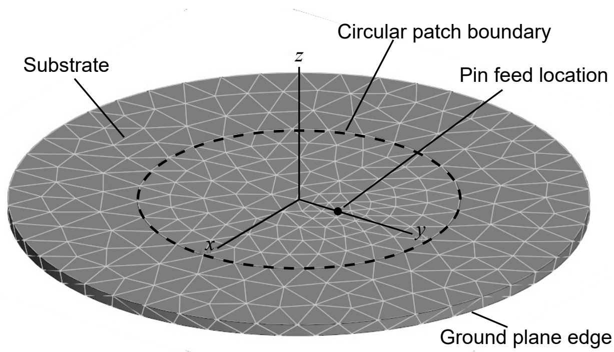

Figure 9.2 Circular patch antenna meshed model for moment method analysis.

substrate, Figure 9.3 shows the simulated z-component of the electric field amplitude in the mid-plane ($z = -H/2$) cross section of the antenna. The electric field minimum occurs along the x axis. The maximum field occurs at symmetric positions along the y axis near the edge of the patch. Fringing field contours are observed to extend beyond the patch edge, which qualitatively shows the characteristic of the effective radius used in Equation (9.11). The simulated input impedance versus frequency is shown in Figure 9.4. Resonance occurs at 1.24 GHz which is in agreement with the predicted value of resonance by Equation (9.10). Assuming a 50-ohm reference impedance, the corresponding simulated reflection coefficient magnitude versus frequency is shown in Figure 9.5, where the minimum value is observed to occur at 1.24 GHz. The next section describes the same type of patch antenna design,

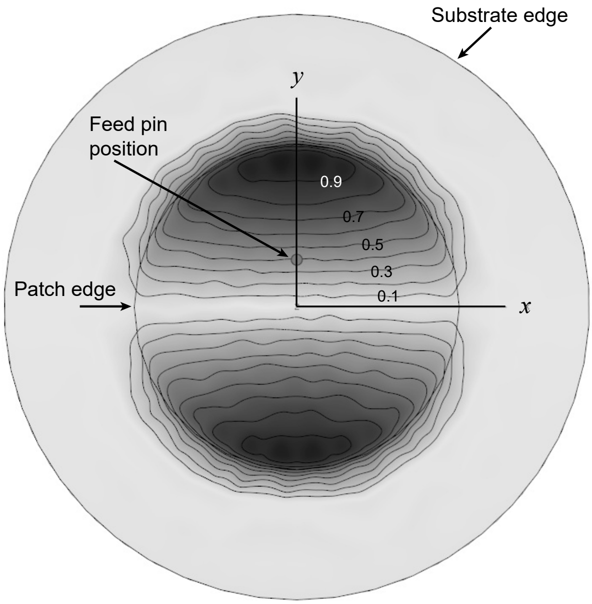

Figure 9.3 Moment method simulated electric field (z component) in the dielectric substrate of the circular patch antenna.

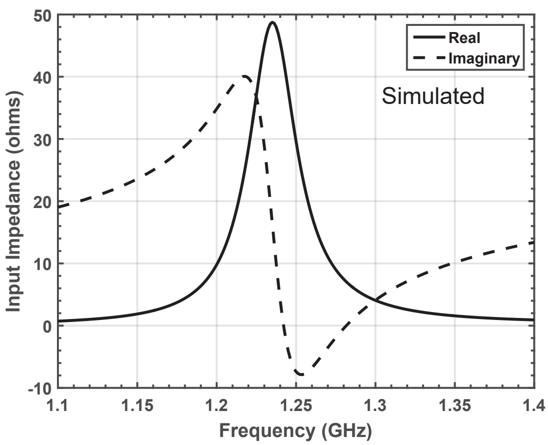

Figure 9.4 Moment method simulated input impedance for the circular patch antenna.

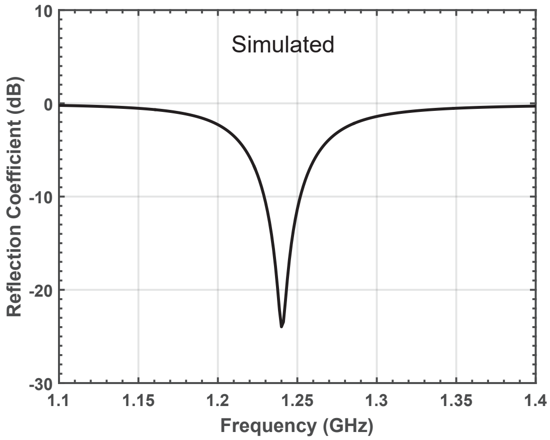

Figure 9.5 Moment method simulated reflection coefficient magnitude for the circular patch antenna.

but now as an element in a non-planar array configuration.

9.4 Non-Planar Array Antenna Design, Simulation Model, and Fabrication

The additive manufactured non-planar patch antenna array design is as follows. The substrate material is assumed to be 0.3175 cm thick ABS-M30 with a measured dielectric constant $\epsilon_r = 2.56$ and loss tangent $\tan\delta = 0.008$ in the range of 1.2 to 1.4 GHz. The chemical name for ABS is Acrylonitrile Butadiene Styrene. The desired resonant frequency was selected as 1.24 GHz. The fabricated patch diameter was 8.46 cm corresponding to the example simulated patch antenna diameter described in Section 9.3. The nonplanar substrate has a radius of curvature 1.128 meters, arc length 1.219 meters, and width 18.034 cm. The array is composed of 10 electrically conducting patch antennas, numbered 1 to 10. The feed-pin arc offset distance s from the center of each patch antenna was 1.232 cm. The array elements had center-to-center arc spacing 12.002 cm, and they were polarized in the E-plane array direction. Figure 9.6 shows a FEKO moment method model of the non-planar array of pin-fed circular patches. The array substrate was designed to be fabricated in two sections that would be bonded together as depicted in Figure 9.7.

An overview of the additive-manufactured array fabrication process is summarized by three photographs in Figure 9.8. The ABS-M30 substrate was 3D printed by RedEye (Eden Prairie, Minnesota, USA) using fused deposition modeling (FDM). The front-surface copper-plated circular antenna

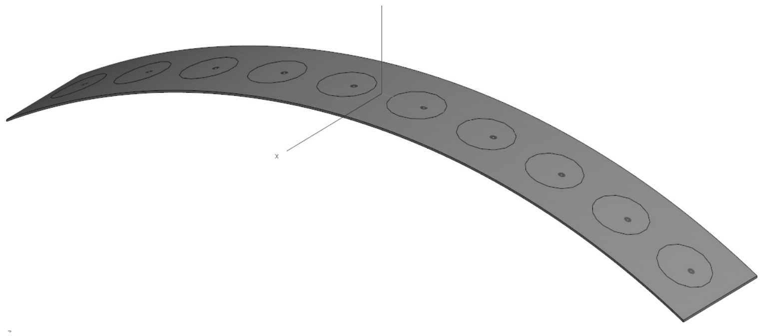

Figure 9.6 Simulation model for a non-planar array of circular patches.

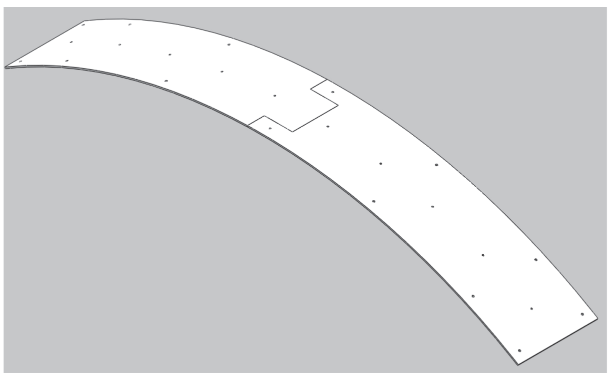

Figure 9.7 Drawing of a non-planar substrate composed of two joined sections.

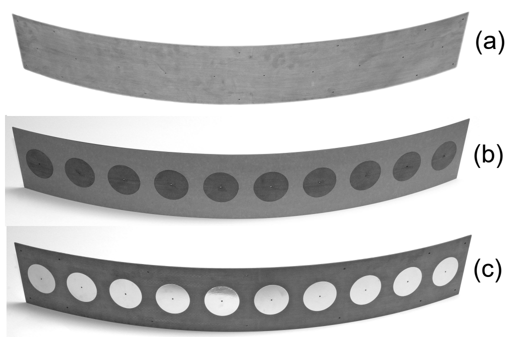

Figure 9.8 Photographs of non-planar array during fabrication. (a) 3D-printed substrate. (b) Substrate with mask for array elements prior to plating. (c) Copper plated array elements on 3D-printed substrate.

elements (8.46 cm diameter) and rear-surface plated-copper ground plane were fabricated by RePliForm (Baltimore, Maryland, USA). The 3D printing process used a T12 extrusion tip with a resolution of 0.1778 mm [0.007 inches]. A photograph of the fabricated ABS-M30 substrate prior to plating is shown in Figure 9.8(a). Due to the fused deposition modeling (FDM) process, tiny air pockets can exist in the 3D-printed material. These air pockets have the potential to allow some of the plating tank material to enter into the 3D-printed substrate and alter the dielectric properties. An acetone vapor treatment was used to seal the 3D-printed ABS substrate, and the substrate surface was lightly sanded to prepare for electroplating. To prepare for copper plating of the patch elements, the substrate was masked as shown in Figure 9.8(b). The final copper plated patch array is shown in Figure 9.8(c). A 3D-printed ABS-M30 support structure was attached to the array backside to maintain the array shape during handling and anechoic chamber measurements. The patch antennas were pin fed using SMA coaxial connectors that were electrically connected to the patch antennas and ground plane using silver epoxy. A photograph of the 3D-printed non-planar array under test is shown in Figure 9.9. Coherent element gain radiation pattern

Figure 9.9 3D-printed non-planar array under test.

measurements were performed with the antenna mounted on a foam column in a tapered anechoic chamber at a range distance of 8.5m [24].

The central eight elements were considered the active array, with one 50-ohm terminated element at each edge (elements 1 and 10). Embedded element performance was simulated and measured with the surrounding elements terminated in 50-ohm resistive loads. Array radiation patterns were computed from the central eight element gain and phase patterns by superposition (summation) using phase conjugation at each scan angle.

9.5 Measured and Simulated Results

Measurements and simulations of the non-planar array were performed with one element driven and the surrounding elements terminated in 50-ohm resistive loads. A comparison of the measured and simulated reflection coefficients for central element number 5 is shown in Figure 9.10 and good agreement is observed. The measured and simulated minimum reflection coefficient (resonance) occurs at 1.23 GHz and 1.24 GHz, respectively, which agree within 1%. The −10 dB reflection coefficient bandwidth is approximately 20 MHz or 1.6%. The corresponding measured and simulated mismatch loss for the central element number 5 is shown in Figure 9.11.

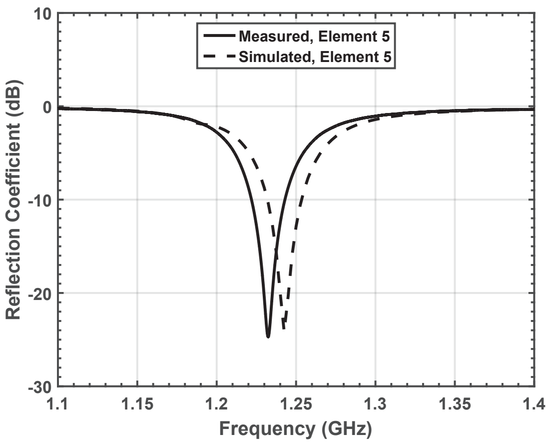

Figure 9.10 Comparison of measured and simulated reflection coefficient magnitude for central element number 5 in the 3D-printed non-planar array.

Element gain patterns for elements 2 to 9 were measured with the surrounding elements terminated in 50-ohm resistive loads. A comparison of the measured and simulated E-plane gain radiation patterns for central element number 5 in the array is shown in Figure 9.12. The central element number 5 peak gain is 4.9 dBi simulated compared to 4.7 dBi measured. A comparison of the measured and simulated E-plane gain radiation patterns for near-edge element number 2 is shown in Figure 9.13. Both the central element and edge element exhibit a broad radiation pattern that allows wide-angle scanning. Referring to Equation (2.63), the coherent embedded element gain patterns were combined by superposition with uniform amplitude illumination to form scanned radiation patterns. Figure 9.14 shows a comparison of measured and simulated E-plane normalized radiation patterns for broadside scan. Figure 9.15 shows a comparison of measured and simulated E-plane

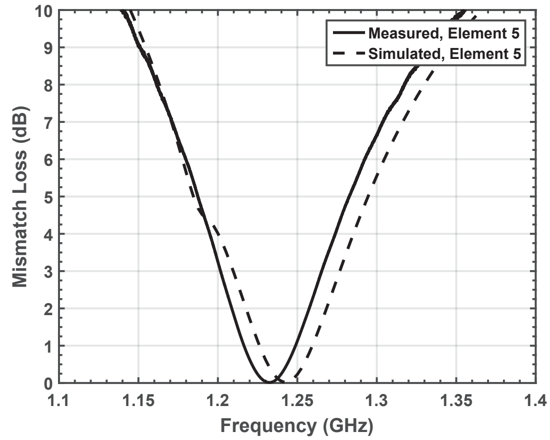

Figure 9.11 Comparison of measured and simulated mismatch loss for central element number 5 in the 3D-printed non-planar array.

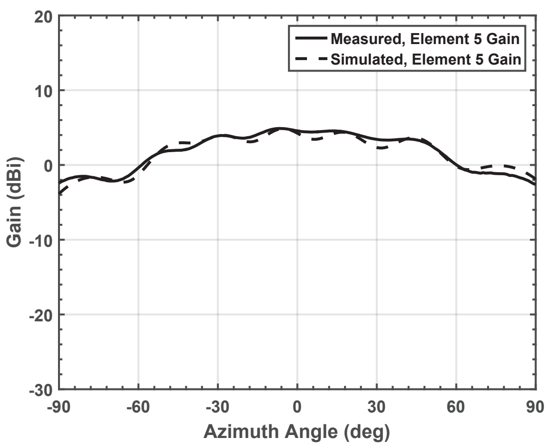

Figure 9.12 Comparison of measured and simulated E-plane gain radiation patterns for central element number 5 in the 3D-printed non-planar array.

normalized radiation patterns for 30° scan. Good agreement between the measurements and simulations is observed in the scanned main beam and sidelobe regions.

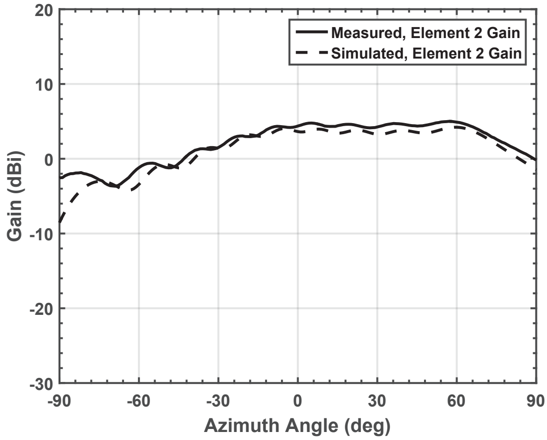

Figure 9.13 Comparison of measured and simulated E-plane gain radiation patterns for near-edge element number 2 in the 3D-printed non-planar array.

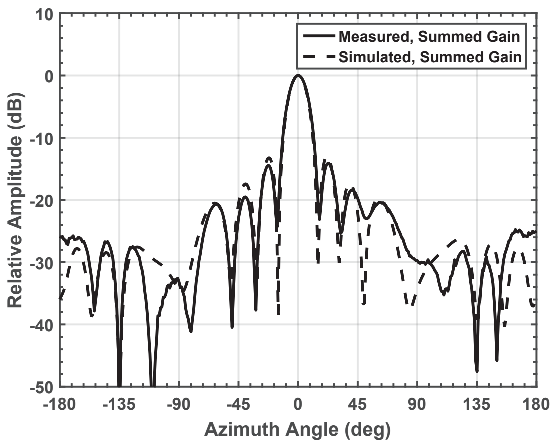

Figure 9.14 Comparison of measured and simulated E-plane normalized radiation patterns of the 3D-printed non-planar array for broadside scan.

9.6 Summary

The theory for circular patch antennas has been reviewed in this chapter. A non-planar circular patch array antenna has been described that uses additive manufacturing with a combination of 3D printer and copper-plating techniques. Measured and simulated array element reflection coefficient, element gain patterns, and scanned beam radiation patterns are in good agreement.

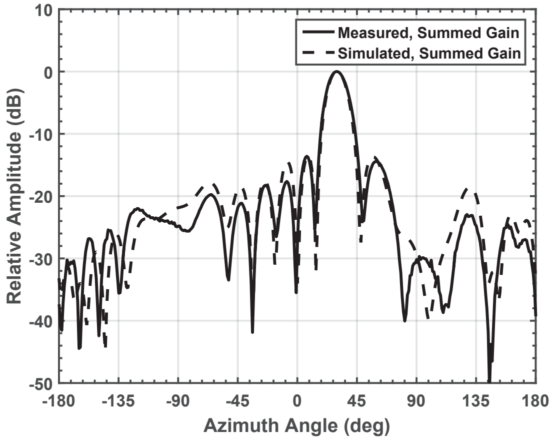

Figure 9.15 Comparison of measured and simulated E-plane normalized radiation patterns of the 3D-printed non-planar array for 30° scan from broadside.

References

[1] D.M. Pozar and D.H. Schaubert, *Microstrip Antennas: The Analysis and Design of Microstrip Antennas and Arrays,* New York: IEEE Press, 1995.

[2] A. K. Bhattacharjee, S. R. Bhadra Chaudhuri, D. R. Poddar, S. K. Chowdhury, "Equivalence of Impedance and Radiation Properties of Square and Circular Microstrip Patch Antennas," *IEE Proceedings H - Microwaves, Antennas and Propagation,* vol. 136, no. 4, 1989, pp. 338 – 342.

[3] I. Wolff and N. Knoppik, "Rectangular and Circular Microstrip Disk Capacitors," *IEEE Trans. on Microwave Theory and Techniques,* vol. MTT-22, no. 10, October 1974, pp. 857–864.

[4] L.C. Shen, S.A. Long, M.R. Allerding, and M.D. Walton, "Resonant Frequency of a Circular Disc, Printed-Circuit Antenna," *IEEE Trans. Antennas and Propagat.*, Vol. 25, 1977, pp. 595–596.

[5] L.C. Shen, "Analysis of a Circular-Disc Printed-Circuit Antenna," *Proc. IEE*, Vol. 126, no. 12, 1979, pp. 1220–1222.

[6] A.G. Derneryd, Analysis of the Microstrip Disk Antenna Element, *IEEE Trans. Antennas and Propagat.*, Vol. 27, 1979, pp. 660–664.

[7] J. Watkins, "Circular Resonant Structures in Microstrip," *Electron Letters,* vol. 5, October 1969, pp. 524–525.

[8] J.J. Adams, E.B. Duoss, T.F. Malkowski, M.J. Motala, B.Y. Ahn, R.G. Nuzzo, J.T. Bernhard, and J.A. Lewis, "Conformal Printing of Electrically Small Antennas on Three-Dimensional Surfaces," *Advanced Materials,* vol. 23, no. 11, 2011, pp. 1335–1340.

[9] E. MacDonald, R. Salas, D. Espalin, M. Perez, E. Aguilera, D. Muse, R.B. Wicker, "3D Printing for the Rapid Prototyping of Structural Electronics," *Access, IEEE,* vol.2, Dec. 2014, pp.234–242.

[10] M. Ahmadloo, "Design and Fabrication of Geometrically Complicated Multiband Microwave Devices Using a Novel Integrated 3D Printing Technique," *IEEE Electrical Performance of Electronic Packaging and Systems (EPEPS) Conference,* San Jose, CA, 2013, pp. 29–32.

[11] G. Shaker, H-S. Lee, S. Safavi-Naeini, M. Tentzeris, "Printed Electronics for Next Generation Wireless Devices", *IEEE Loughborough Antennas and Propagation Conference (LAPC),* November 2011, pp. 1–5.

[12] J. Mei, M. Lovell, and M. Mickle, "Formulation and Processing of Novel Conductive Solution inks in Continuous Inkjet Printing of 3-D Electric Circuits," *IEEE Transactions on Electronics Packaging Manufacturing,* vol. 28, no. 3, July 2005, pp. 265–273.

[13] G. Shaker, S. Safavi-Naeini, N. Sangary, and M. Tentzeris, "Inkjet Printing of Ultrawideband (UWB) Antennas on Paper-based Substrates", *IEEE Antennas and Wireless Propagation Letters,* Vol. 10, 2011, pp. 111–114.

[14] J. Siden, M. Fein, A. Koptyug, and H. Nilsson, "Printed Antennas with Variable Conductive Ink Layer thickness", *IET Microwaves, Antennas Propagat.,* vol. 1, no. 2, April 2007, pp. 401–407.

[15] J. Mei, M.R. Lovell, and M.H. Mickle, "Formulation and Processing of Novel Conductive Solution Inks in Continuous Inkjet Printing of 3-D Electric Circuits," *IEEE Trans. on Electronics Packaging,* vol. 28, no. 3, July 2005, pp. 265–273.

[16] M. Ahmadloo, and P. Mousavi, "A Novel Integrated Dielectric-and-Conductive Ink 3D Printing Technique for Fabrication of Microwave Devices", *IEEE MTT International Microwave Symposium (IMS) 2013,* Seattle, June 2–7, 2013.

[17] M. Ahmadloo, and P. Mousavi, "Application of Novel Integrated Dielectric and Conductive Ink 3D Printing Technique for Fabrication of Conical Spiral Antennas", *IEEE APS/USNC-URSI 2013,* Orlando, Florida, July 7–13, 2013.

[18] K.A. Nate, J. Hester, M. Isakov, R. Bahr, M.M. Tentzeris, "A Fully Printed Multilayer Aperture-Coupled Patch Antenna Using Hybrid 3D / Inkjet Additive Manufacturing Technique," *Proc. of the 45th European Microwave Conference,* 7–10 Sept 2015, Paris, France, pp. 610–613.

[19] A.J. Fenn, D.J. Pippin, D. Hogan, C.M. Lamb, F.G. Willwerth, H.M. Aumann, J.P. Doane, "3D Printed Conformal Array Antenna: Simulations and Measurements," *2016 IEEE International Symposium on Phased Array Systems and Technology,* Waltham, MA: October 2016.

[20] M.W. Elsallal, J. Hood and I. McMichael, T. Busbee, "3D Printed Material Characterization for Complex Phased Arrays and Metamaterials," *Microwave Journal*, October 14, 2016.

[21] S.D. Gupta, "Effect of Mutual Coupling in E and H Plane on Microstrip Antenna Array Conformal on Cylindrical Surface," *2013 Int. Conf. on Signal Processing and Communication,* 12–14 Dec. 2013, pp. 149–154.

[22] G.N. Watson, *A Treatise on the Theory of Bessel Functions*, London: Cambridge University Press, 1966, p. 17.

[23] A.Z. Elsherbeni, P. Nayeri, and C. J. Reddy, *Antenna Analysis and Design Using FEKO Electromagnetic Simulation Software,* Edison, New Jersey: SciTech Publishing, 2014.

[24] A.J. Fenn, M.W. Shields, and G.A. Somers, "Introduction to the new MIT Lincoln Laboratory suite of ranges," *26th Annual Antenna Measurement Techniques Association Meeting & Symposium, AMTA 2004,* Stone Mountain Park, Georgia, 17–22 October 2004.